

Strong shape dependence of the Morin transition in α -Fe₂O₃ single-crystalline nanostructures

Jun Wang^{1,a}, Victor Aguilar², Le Li¹, Fa-gen Li¹, Wen-zhong Wang³, and Guo-meng Zhao^{1,2,b}

¹*Department of Physics, Faculty of Science,
Ningbo University, Ningbo, P. R. China*

²*Department of Physics and Astronomy,
California State University, Los Angeles, CA 90032, USA*

³*School of Science, Minzu University of China, Beijing 100081, P. R. China*

Abstract

Single-crystalline α -Fe₂O₃ nanorings (short nanotubes) and nanotubes were synthesized by a hydrothermal method. High-resolution transmission electron microscope and selected-area electron diffraction confirm that the axial directions of both nanorings and nanotubes are parallel to the crystalline *c*-axis. What is intriguing is that the Morin transition occurs at about 210 K in the short nanotubes with a mean tube length of about 115 nm and a mean outer diameter of 169 nm while it disappears in the nanotubes with a mean tube length of about 317 nm and a mean outer diameter of 148 nm. Detailed analyses of magnetization data, x-ray diffraction spectra, and room-temperature Mössbauer spectra demonstrate that this very strong shape dependence of the Morin transition is intrinsic to hematite. We can quantitatively explain this intriguing shape dependence in terms of opposite signs of the surface magnetic anisotropy constants in the surface planes parallel and perpendicular to the *c*-axis (that is, $K_{s\parallel} = -0.37$ erg/cm² and $K_{s\perp} = 0.42$ erg/cm²).

I. INTRODUCTION

Hematite ($\alpha\text{-Fe}_2\text{O}_3$) has a corundum crystal structure and orders antiferromagnetically below its Néel temperature of about 960 K. Bulk hematite exhibits a Morin transition¹ at about 260 K, below which it is in an antiferromagnetic (AF) phase, where the two antiparallel sublattice spins are aligned along the rhombohedral [111] axis. Above the Morin transition temperature T_M , $\alpha\text{-Fe}_2\text{O}_3$ is in the weak ferromagnetic (WF) phase, where the antiparallel spins are slightly canted and lie in the basal (111) plane rather than along [111] axis. The Morin transition is accompanied by the change of the total magnetic anisotropic constant from a negative value at $T > T_M$ to a positive value at $T < T_M$. Interestingly, this AF-WF transition was found to depend on magnetic field. An applied magnetic field parallel to the rhombohedral [111] axis below T_M was shown²⁻⁴ to induce the spin-flip transition in the entire temperature range below T_M . The AF-WF transition can also be induced by an applied magnetic field perpendicular to the [111] direction⁵. The magnetic structure, the Morin transition, and the field dependence of T_M were explained^{5,6} in terms of phenomenological thermodynamical potential of Dzyaloshinsky.

In recent years, magnetic nanostructures have attracted much attention, not only because of their interesting physical properties but also because of their broad technological applications. Of particular interest is a finite-size effect on ferromagnetic/ferrimagnetic transition temperature. Finite-size effects have been studied in quasi-two-dimensional ultra-thin ferromagnetic films⁷⁻¹⁰ and in quasi-zero-dimensional ultra-fine ferromagnetic/ferrimagnetic nanoparticles¹¹⁻¹⁵. The studies on thin films⁷⁻¹⁰ and recent studies on nanoparticles¹³⁻¹⁵ have consistently confirmed the finite-size scaling relationship predicted earlier¹⁶. Similarly, a finite-size effect on the Morin transition temperature was observed in nanosized $\alpha\text{-Fe}_2\text{O}_3$ spherical particles¹⁷⁻²¹. The data show that T_M decreases with decreasing particle size^{17,19}, similar to the case of ferromagnetic/ferrimagnetic nanoparticles¹³⁻¹⁵. The reduction in the Morin transition temperature was interpreted as due to inherent lattice strain (lattice expansion) of nano-crystals^{17,20}. It was also shown¹⁹ that the T_M suppression is caused by both strain and the finite-size effect, commonly observed in ferromagnetic/ferrimagnetic materials. More recently, Mitra *et al.*²² have found that T_M shifts from 251 K for ellipsoidal to 221 K for rhombohedral nanostructure, which suggests observable shape dependence of the Morin transition. Here we show that the Morin transition temperature depends very strongly on the shape of nanocrystals: T_M shifts from 210 K for the nanorings (short nan-

otubes with a mean tube length of about 115 nm) to <10 K for the nanotubes with a mean tube length of about 317 nm. The very strong shape dependence of the Morin transition is quite intriguing considering the fact that the lattice strains of both nanoring and nanotube crystals are negligibly small, and that the sizes of nanotubes are too large to explain their complete suppression of T_M by a finite-size effect. Instead, we can quantitatively explain this intriguing shape dependence in terms of opposite signs of the surface magnetic anisotropy constants in the surface planes parallel and perpendicular to the c -axis.

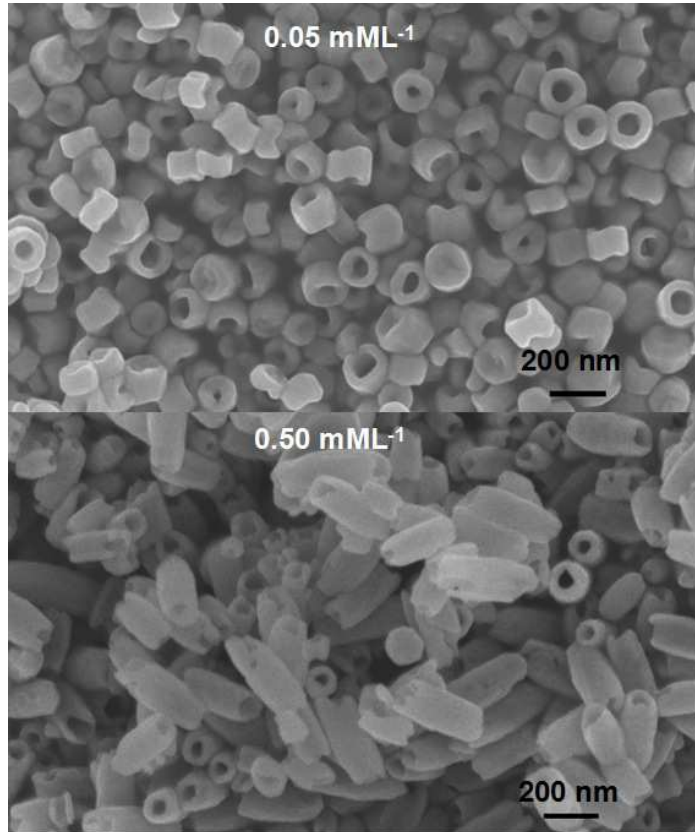


FIG. 1: Scanning electron microscopic images of the two α -Fe₂O₃ nanostructures prepared with different phosphate concentrations. A ring-like morphology (short nanotubes) is seen in the sample prepared with the phosphate concentration of 0.05 mM/L (upper panel) and a tube-like morphology is observed in the sample prepared with the phosphate concentration of 0.50 mM/L (lower panel).

II. EXPERIMENTAL RESULTS

α -Fe₂O₃ nanorings were prepared by a hydrothermal method, which is similar to that reported in²³. In the typical process, FeCl₃, NH₄H₂PO₄ (phosphate), and Na₂SO₄ were

dissolved in deionized water with concentrations of 0.002, 0.05 and 0.55 mM/L, respectively. After vigorous stirring for 15 min, the mixture was transferred into a Teflon-lined stainless steel autoclave for hydrothermal treatment at 240 °C for 48 h. While keeping all other experimental parameters unchanged, increasing the phosphate concentration from 0.05 to 0.50 mM/L to produce nanotubes.

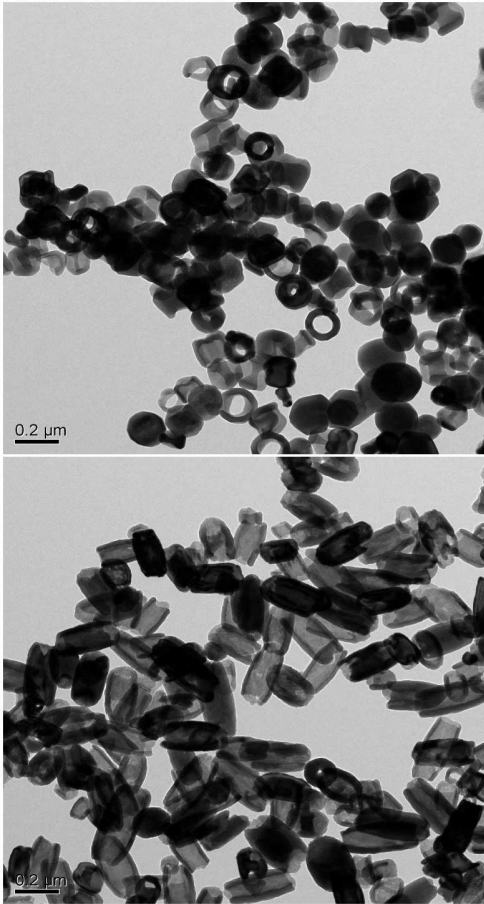


FIG. 2: Transmission electron microscopic images of the two α - Fe_2O_3 nanostructures. The upper panel is the image for the nanorings and the lower panel is for the nanotubes.

The morphology of the samples was analyzed by field emission scanning electron microscopy (FE-SEM, SU70, operated at 3 kV) and transmission electron microscopy (JEOL-2010, operated at 200 kV). Figure 1 shows scanning electron microscopic (SEM) images of the two α - Fe_2O_3 nanostructures prepared with different phosphate concentrations. A ring-like morphology is seen in the sample prepared with the phosphate concentration of 0.05 mM/L (upper panel) and a tube-like morphology is observed in the sample prepared with the phosphate concentration of 0.50 mM/L (lower panel). In fact, these nanorings can be described as short nanotubes with tube lengths shorter than outer diameters.

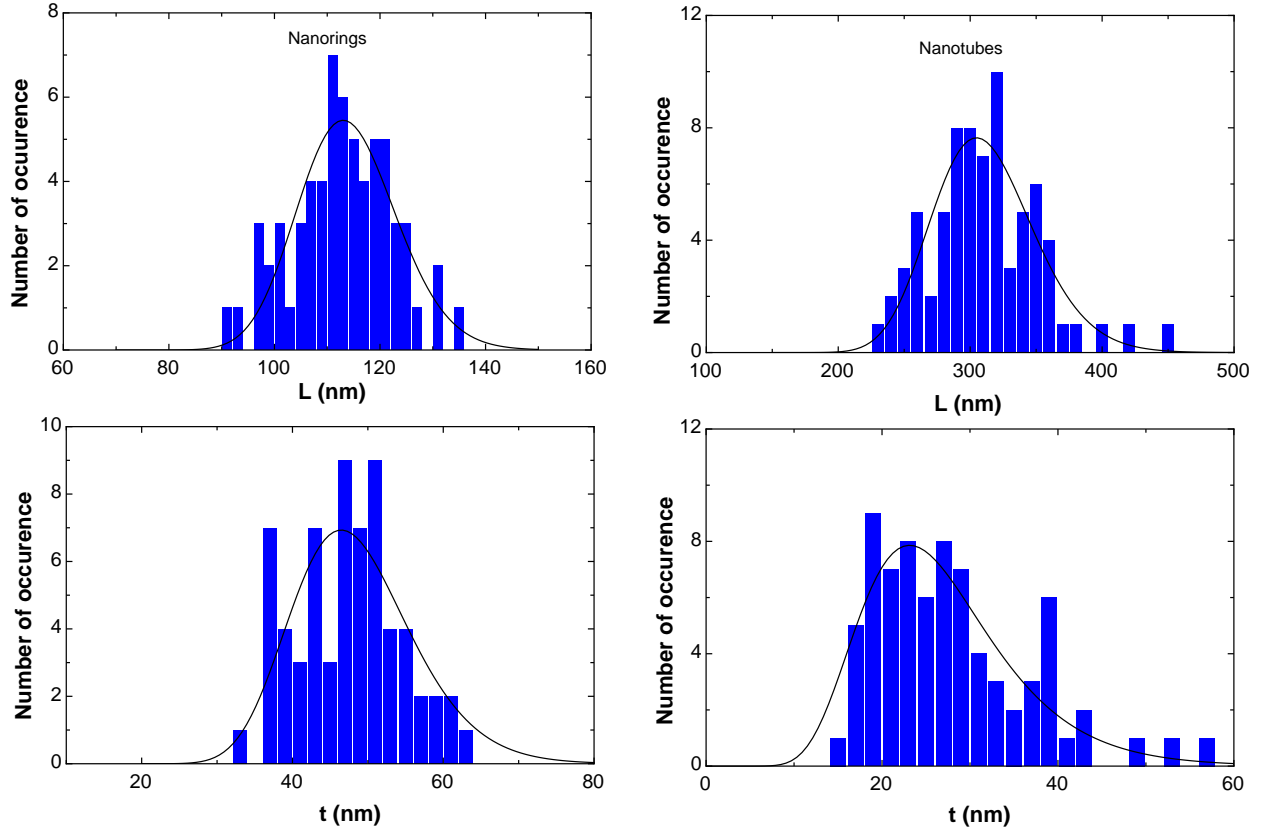


FIG. 3: Length (L) and wall-thickness (t) histograms of the nanorings (left panel) and nanotubes (right panel). The solid lines are the best fitted curves by log-normal distribution functions.

The transmission electron microscopic (TEM) images for the two samples are displayed in Fig. 2. The upper panel is the TEM image for the nanorings and the lower panel is for the nanotubes. The TEM images show much clearer morphologies of the nanocrystals than the SEM images, which allow us to obtain histograms of their lengths and wall thicknesses. The histograms for the two samples are displayed in Fig. 3. Both length and thickness distributions are well described by a log-normal distribution function:

$$P(x) = \frac{1}{x\sigma\sqrt{2\pi}} \exp\left(-\frac{\ln^2(x/x_0)}{2\sigma^2}\right), \quad (1)$$

where σ is the standard deviation and $\ln x_0$ is the mean value of $\ln x$. The best fit of Eq. 1 to the data yields $L_0 = 113.8 \pm 0.9$ nm and $t_0 = 47.8 \pm 1.3$ nm for the nanorings, and $L_0 = 309.5 \pm 3.7$ nm and $t_0 = 25.6 \pm 0.9$ nm for the nanotubes.

Since x-ray diffraction intensity or magnetic moment of a particle is proportional to its volume, the mean value of length or thickness should be length- or thickness-weighted, that

is,

$$x_{av} = \frac{\int_0^\infty x^2 P(x) dx}{\int_0^\infty x P(x)}. \quad (2)$$

Based on Eq. 2 and the fitting parameters for the histograms, the mean length and thickness are calculated to be 115 and 50 nm for the nanorings, respectively, and 317 and 30 nm for the nanotubes, respectively. The mean outer diameter of the short nanotubes are 169 nm, much larger than the mean tube length (115 nm), which is consistent with the ring morphology. The mean outer diameter of the nanotubes are 148 nm, much smaller than the mean tube length (317 nm), which is consistent with the tube morphology. It is remarkable that the mean thicknesses (50 and 30 nm) of the nanorings and nanotubes inferred from the TEM images are very close to those (58 and 32 nm) deduced from x-ray diffraction spectra (see below).

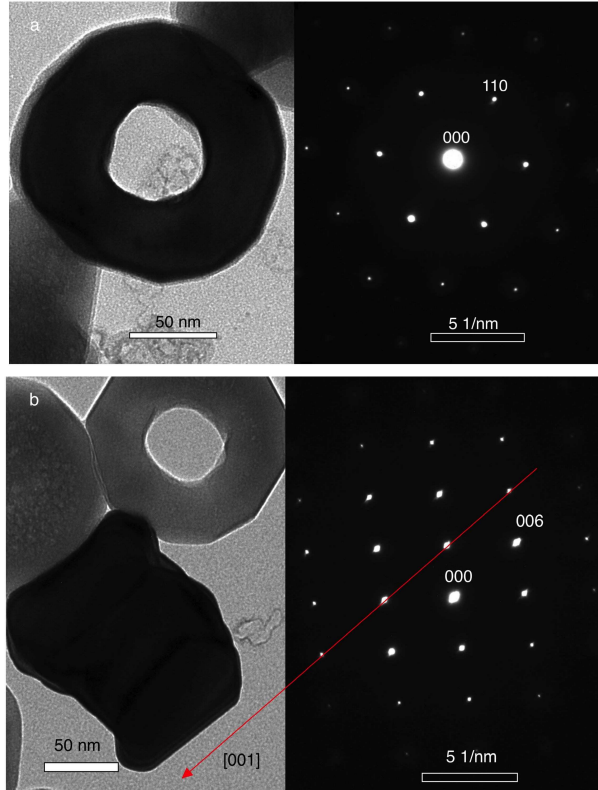


FIG. 4: TEM images (left panels) and SAED patterns (right panels) for a single nanoring. The results consistently demonstrate the single-crystalline nature of the nanoring with its axis parallel to the [001] direction.

In the left panel of Figure 4a, we show the TEM image of a single nanoring (the top view). This ring has a wall thickness of about 50 nm, which is very close to the mean value deduced from the histogram above and slightly smaller than the mean value of 58 nm deduced from

the XRD peak widths (see below). The selected-area electron diffraction (SAED) pattern (right panel of Fig. 4a) with a clear hexagonal symmetry indicates that the nanoring is a single crystal with a ring axis parallel to the crystalline *c*-axis. In order to further prove the single-crystalline nature of the nanoring, we show the side-wall view of the ring (left panel of Fig. 4b) and the corresponding SAED pattern (right panel of Fig. 4b). The red arrow indicates the [001] direction, which is determined by the SAED pattern. It is apparent that the ring axis is parallel to the [001] direction or the crystalline *c*-axis. From the SAED pattern, we can evaluate the *c*-axis lattice constant. The obtained $c = 13.77(2)$ Å is close to that determined from the XRD data (see below).

For the nanotube sample, it is very unlikely to get a top-view TEM image since the axes of the tubes tend to be parallel to the surface of the sample substrate. So we can only take TEM images of a single nanotube from the side-wall view. The left panel of Fig. 5 displays a side-wall-view TEM image of a nanotube. The image indicates that the length of the tube is about 200 nm. The single-crystalline nature of the nanotube is clearly confirmed by the SAED pattern (see the right panel of Fig. 5). The red arrow marks the [001] direction, which is determined by the SAED pattern. It is striking that the tube axis is also parallel to the [001] direction.

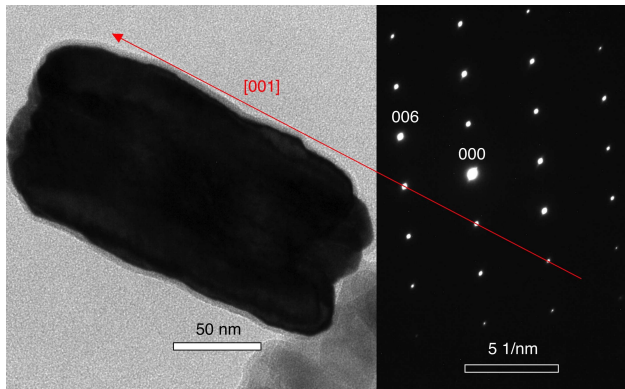


FIG. 5: TEM image (left panel) and SAED pattern (right panel) for a single nanotube. The results consistently demonstrate the single-crystalline nature of the nanotube with its axis parallel to the [001] direction.

Figure 6 shows x-ray diffraction (XRD) spectra of two α -Fe₂O₃ nanostructures prepared with the NH₄H₂PO₄ concentrations of 0.05 and 0.50 mM/L, respectively. The spectra were taken by Rigaku Rint D/Max-2400 X-ray diffractometer. These samples are phase pure, as the spectra do not show any traces of other phases. Rietveld refinement of the XRD

data (see solid blue lines) with a space group of $R\bar{3}c$ (trigonal hematite lattice) was carried out to obtain the cell parameters and fractional coordinates of the atoms. The atomic occupancy was assumed to be 1.0 and not included in the refinement. We tried to include the lattice strains and particle sizes in the refinement but the uncertainties of these fitting parameters are even much larger than themselves. A large reliability factor ($R_{wp} \sim 11\%$) of the refinement makes it impossible to yield reliable fitting parameters for lattice strains (which are negligibly small) and particle sizes (which are quite large). In contrast, the lattice parameters obtained from the refinements are quite accurate: $a = b = 5.0311(12)$ Å, $c = 13.7760(33)$ Å for the nanotube sample, and $a = b = 5.0340(6)$ Å, $c = 13.7635(17)$ Å for the nanoring sample. These parameters are slightly different from those for a bulk hematite²⁴: $a = b = 5.0351$ Å, $c = 13.7581$ Å.

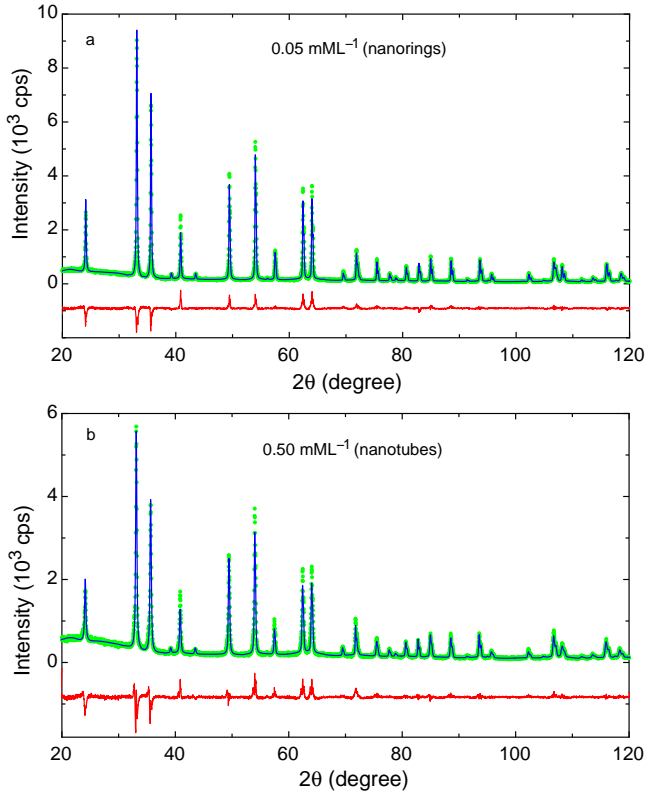


FIG. 6: X-ray diffraction (XRD) spectra of two α - Fe_2O_3 nanostructures prepared with the $\text{NH}_4\text{H}_2\text{PO}_4$ concentrations of 0.05 and 0.50 mM/L, respectively. Rietveld refinement of the XRD data (solid blue lines) with a space group of $R\bar{3}c$ (trigonal hematite lattice) was carried out to obtain the lattice parameters and fractional coordinates of the atoms. The red lines represent the differences between the data and the refined curves.

Since the axes of both nanorings and nanotubes are parallel to the crystalline c -axis, the

mean wall thickness of the nanorings and nanotubes can be quantitatively determined by the peak widths of the x-ray diffraction peaks that are associated with the diffraction from the planes perpendicular to the c -axis. Figure 7 shows x-ray diffraction spectra of the (110), (300), and (220) peaks for the nanoring and nanotube samples. The peaks are best fitted by two Lorentzians (solid lines) contributed from the Cu $K_{\alpha 1}$ and $K_{\alpha 2}$ radiations. The fit has a constraint that the ratio of the $K_{\alpha 1}$ and $K_{\alpha 2}$ intensities is always equal to 2.0, the same as that used in Rietveld refinement.

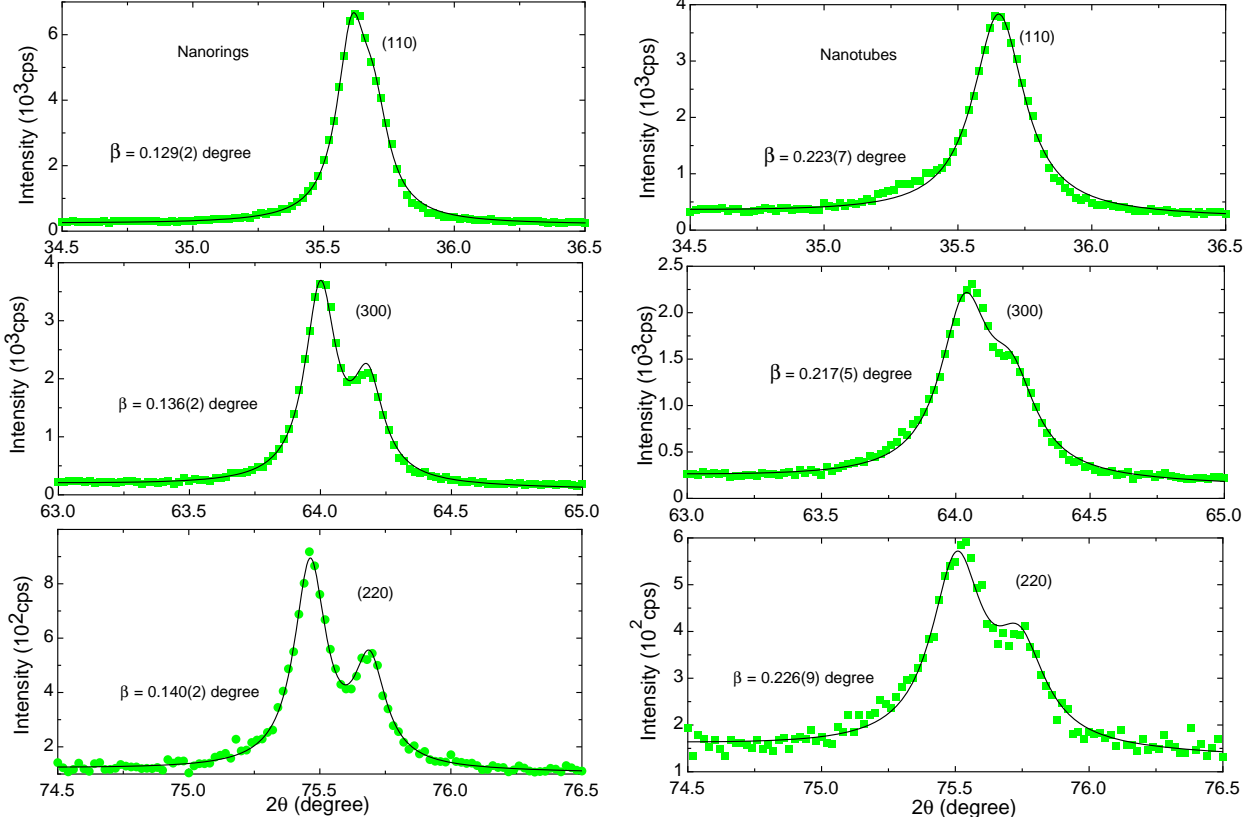


FIG. 7: X-ray diffraction spectra of the (110), (300), and (220) peaks for the nanorings (left panel) and nanotubes (right panel). The peaks are best fitted by two Lorentzians (solid lines), which are contributed from the Cu $K_{\alpha 1}$ and $K_{\alpha 2}$ radiations. The intrinsic peak width β (after correcting for the instrumental broadening) is indicated in each figure.

It is known that the x-ray diffraction peaks are broadened by strain, lattice deficiencies, and small particle size. When the density of lattice deficiencies is negligibly small, the broadening is contributed from both strain ϵ and particle size t_{av} . In this case, there is a simple expression²⁵:

$$\frac{\beta \cos \theta}{\lambda} = \frac{0.89}{t_{av}} + \frac{2\xi \sin \theta}{\lambda}, \quad (3)$$

where the first term is the same as Scherrer's equation that is related to the particle size t_{av} , the second term is due to strain broadening, and ξ was found to be close to 2ϵ (Ref.²⁶). In Fig. 8, we plot $\beta \cos \theta / \lambda$ versus $2 \sin \theta / \lambda$ for the nanorings and nanotubes. According to Eq. 3, a linear fit to the data gives information about the mean wall thickness t_{av} and strain ϵ_a along a and b axes. The strain is small and negative for both samples (see the numbers indicated in the figures). It is interesting that the magnitudes of the strain inferred from the XRD peak widths are very close to those calculated directly from the measured lattice parameters. For example, the strain is calculated to be $-0.023(13)\%$ from the lattice parameters for the nanorings and for the bulk, in excellent agreement with that $(-0.017(2)\%)$ inferred from the XRD peak widths. Moreover, the mean wall thicknesses inferred from the XRD peak widths are very close to those determined from TEM images. This further justifies the validity of our Williamson-Hall analysis of the XRD peak widths.

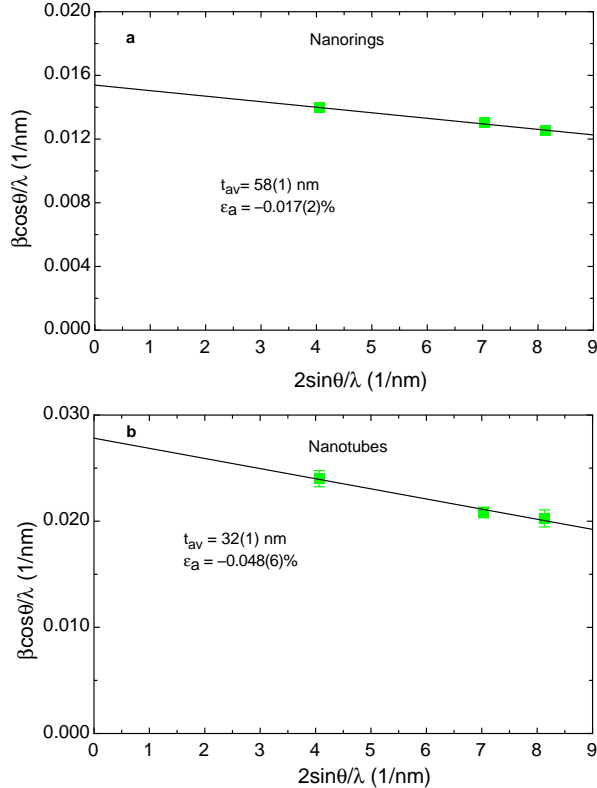


FIG. 8: Dependence of $\beta \cos \theta / \lambda$ on $2 \sin \theta / \lambda$ for the nanorings and nanotubes. The linear lines are the fitted curves by Eq. 3. The fitting parameters are indicated in each figure. The error bars in (a) are inside the symbols and not visible.

Figure 9 shows temperature and field dependences of the normalized magnetizations $M(T)/M(350K)$ for the $\alpha\text{-Fe}_2\text{O}_3$ single-crystalline nanorings and nanotubes. Magnetic mo-

ment was measured using a Quantum Design vibrating sample magnetometer (VSM) with a resolution better than 1×10^{-6} emu. The samples were initially cooled to 10 K in zero field and a field of 100 Oe was set at 10 K, and then the moment was taken upon warming up to 350 K and cooling down from 350 K to 10 K. At 10 K, other higher fields (1 kOe, 10 kOe, and 50 kOe) were set and the moment was taken upon warming up to 350 K and cooling down from 350 K to 10 K. It is remarkable that the magnetic behaviors of the two nanostructures are very different. For the nanorings, the magnetization shows rapid increase around 200 K upon warming, which is associated with the Morin transition (see Fig. 9a). It is worth noting that there seem to be two transitions with slightly different Morin transition temperatures. The reason for this is unclear.

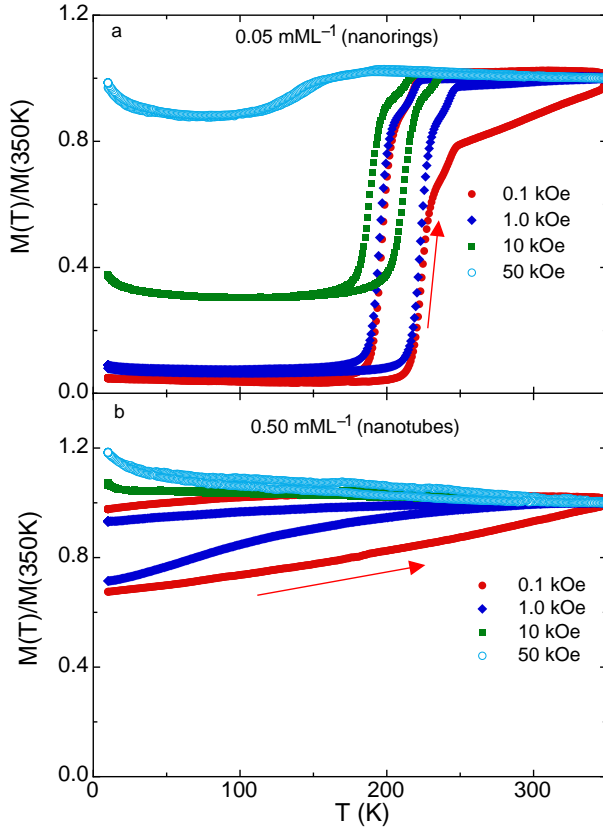


FIG. 9: Temperature and field dependencies of the normalized magnetizations $M(T)/M(350K)$ for the nanorings (a) and nanotubes (b). For the nanotubes, the normalized magnetization measured in a lower field (10 Oe) is very similar to that measured in 100 Oe, suggesting absence of the Morin transition down to this low field.

Furthermore, the magnetization below the Morin transition temperature T_M is small (AF state) and it enhances significantly above T_M (WF state). It is interesting that T_M for heating measurements is significantly higher than that for cooling measurements (the arrows

in the figure indicate the directions of the measurements). This difference is far larger than a difference (about 6 K) due to extrinsic thermal lag. This thermal hysteresis was also observed in spherical α -Fe₂O₃ nanoparticles¹⁹. The observed intrinsic thermal hysteresis shows that the nature of the Morin transition is of first-order. The result in Fig. 9a also suggests that the Morin transition temperature decreases with the increase of the applied magnetic field. The zero-field T_M in the nanorings is about 210 K. What is striking is that the Morin transition is almost completely suppressed in the nanotubes (see Fig. 9b).

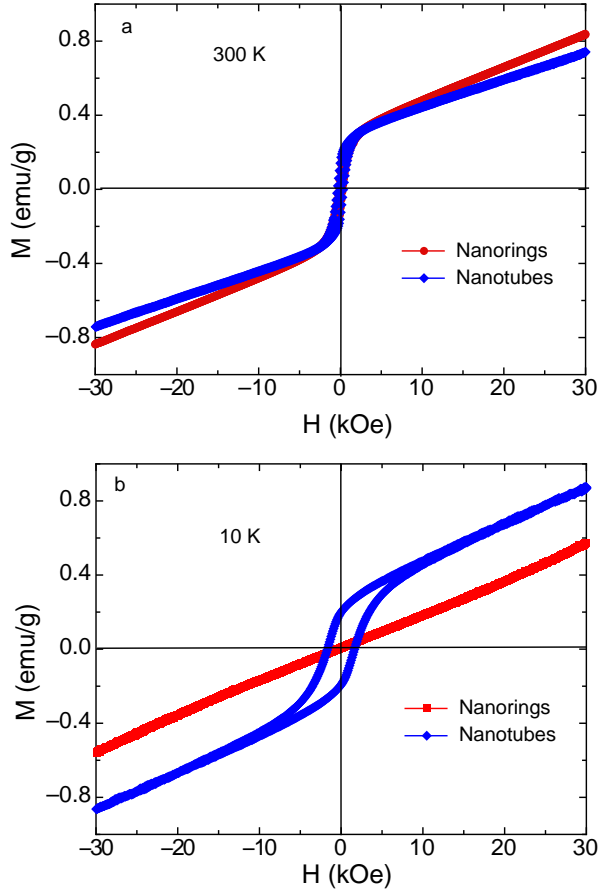


FIG. 10: Magnetic hysteresis loops at 300 K and 10 K for the nanorings and nanotubes. The room-temperature saturation magnetization M_s , as inferred from a linear fit to the magnetization data above 15 kOe, is the same (0.303 ± 0.001 emu/g) for both samples. The saturation magnetizations for both samples are nearly the same as that (0.29 ± 0.02 emu/g)²¹ for a polycrystalline sample with a mean grain size of about 3 μ m.

In Figure 10a, we compare magnetic hysteresis loops at 300 K for the nanorings and nanotubes. There is a subtle difference in the magnetic hysteresis loops of the two samples. The remanent magnetization M_r for the nanotube sample is about 40% higher than that for the

nanoring sample, which is related to a higher coercive field in the former sample. However, the saturation magnetization M_s , as inferred from a linear fit to the magnetization data above 15 kOe, is the same (0.303 ± 0.001 emu/g) for both samples. The saturation magnetizations for both samples are also the same as that (0.29 ± 0.02 emu/g)²¹ for a polycrystalline sample with a mean grain size of about 3 μm . Since the saturation magnetization is very sensitive to the occupancy of the Fe^{3+} site, the fact that the saturation magnetizations of both nanaoring and nanotube samples are nearly the same as the bulk value suggests that the occupancies of the Fe^{3+} site in the nanostructural samples are very close to 1.0, which justifies our XRD Rietveld refinement. Fig. 10b shows magnetic hysteresis loops at 10 K for the two samples. It is clear that the nanotube sample remains weak ferromagnetic at 10 K (the absence of the Morin transition down to 10 K) while the nanoring sample is antiferromagnetic with zero saturation magnetization.

III. DISCUSSION

The completely different magnetic behaviors observed in the nanoring and nanotube samples are intriguing considering the fact that the two samples have the same saturation magnetization at 300 K and nearly the same lattice parameters. It is known that the lattice strain can suppress T_M according to an empirical relation deduced for spherical nanoparticles¹⁹: $\Delta T_M = -600\epsilon$ K, where ϵ is isotropic lattice strain in %. For a uniaxial strain, the formula may be modified as $\Delta T_M = -200\epsilon_i$ K, where ϵ_i is the strain along certain crystalline axis. For the nanoring sample, $a = 5.0340(6)$ Å, which is slightly smaller than (5.0351 Å) for a bulk hematite²⁴. This implies that $\epsilon_a = -0.023(13)\%$ for the nanoring sample, in excellent agreement with that (-0.017(2)% inferred from the XRD peak widths. For the nanotube sample, $a = 5.0311(12)$ Å, so $\epsilon_a = -0.080(24)\%$, in good agreement with that (-0.048(6)% inferred from the XRD peak widths. The negative strain would imply an increase in T_M according to the argument presented in Ref.¹⁷. Therefore the suppression of T_M cannot arise from the lattice strains along the a and b directions. On the other hand, the lattice strain along the c direction is positive. Comparing the measured c -axis lattice parameters of the two samples with that for a bulk hematite²⁴, we can readily calculate that $\epsilon_c = 0.040(12)\%$ for the nanoring sample and $0.130(24)\%$ for the nanotube sample. This would lead to the suppression of T_M by 8(2) K and 26(5) K for the nanoring and nanotube samples, respectively. The small negative strains along a and b directions are compensated

by the positive strain along c direction (also see Table II below) so that the volume of unit cell remains nearly unchanged. This implies that the T_M suppression due to lattice strains should be negligibly small.

As mentioned above, there is also an independent finite-size effect on T_M unrelated to the strain. For spherical nanoparticles, T_M is suppressed according to $\Delta T_M = -1300/d$ K (Ref.¹⁹), where d is the mean diameter of spherical particles in nm. For the nanoring and nanotube samples, the smallest dimension is the wall thickness, which should play a similar role as the diameter of spherical particles¹⁴. With $t_{av} = 58$ nm and 32 nm for the nanoring and nanotube samples, respectively, the suppression of T_M is calculated to be 22 K and 41 K, respectively. Therefore, due to the finite-size effect, T_M would be reduced from the bulk value of 258 K (Ref.¹⁷) to 236 K and 217 K for the nanoring and nanotube samples, respectively. For the nanoring sample, the zero-field T_M is about 211 K, which is 25 K lower than the expected value from the finite-size effect only. This additional T_M suppression of 25 K should be caused by other mechanism discussed below. For the nanotube sample, the Morin transition is almost completely suppressed, which cannot be explained by the strain and/or finite-size effect.

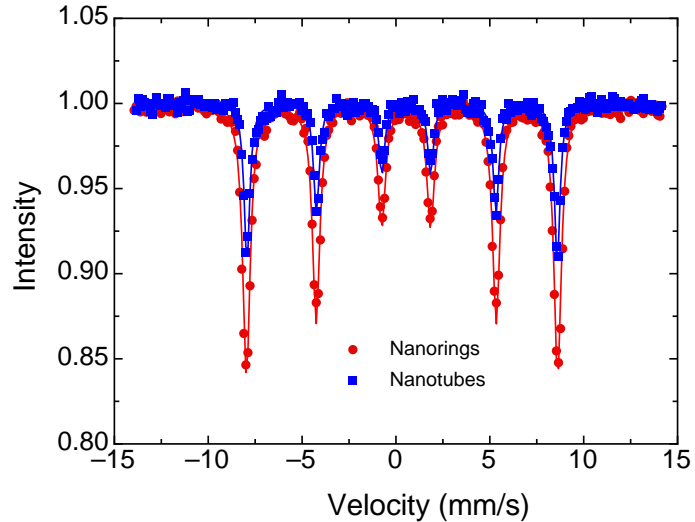


FIG. 11: Room-temperature Mössbauer spectra for the nanorings and nanotubes. The spectra are fitted by a single sextet (solid lines) with the fitting parameters displayed in Table I.

Another possibility is that the nanotubes may contain more lattice deficiencies than the nanorings. If this were true, the line width of the Mössbauer spectrum for the nanotube sample would be broader than that for the nanoring sample because the line width is sensitive to disorder, inhomogeneity, and lattice deficiencies. In contrast, the observed line width for

the nanotube sample is smaller than that for the nanoring sample by 33% (see Fig. 11 and Table I). If there would exist substantial lattice deficiencies, they would mostly be present in surface layers. The narrower Mössbauer line width observed in the nanotube sample is consistent with the fact that the nanotubes have a smaller fraction of surface layers. Moreover, the room-temperature Mössbauer spectra of both samples show only one set of sextet, suggesting no superparamagnetic relaxation at room temperature. This is consistent with the observed magnetic hysteresis loops (see Fig. 10a).

TABLE I: The fitting parameters for the room-temperature Mössbauer spectra of the nanorings and nanotubes

	Half width (mm/s)	Hyperfine field (kOe)	Isomer shifts (mm/s)	Quadrupole shifts (mm/s)
Nanorings	0.240 ± 0.005	513.30 ± 0.20	0.44 ± 0.01	-0.220 ± 0.005
Nanotubes	0.180 ± 0.005	511.85 ± 0.23	0.44 ± 0.01	-0.220 ± 0.005

Finally, we can quantitatively explain the strong shape dependence of the Morin transition temperature if we assume that the surface magnetic anisotropy constant K_s is negative in the surface planes parallel to the c -axis and positive in the surface planes perpendicular to the c -axis. Indeed a negative value of K_s was found in Ni (111) surface²⁷ while K_s is positive in Co(0001) surface²⁸. For the nanorings, the surface area for the planes parallel to the c -axis are similar to that for the planes perpendicular to the c -axis. Therefore, the total K_s will have a small positive or negative value due to a partial cancellation of the K_s values (with opposite signs) in different surface planes. In contrast, the surface area of a nanotube for the surface planes parallel to the c -axis is much larger than that for the planes perpendicular to the c -axis. This implies that the total K_s in the nanotubes should have a large negative value.

For bulk hematite, the Morin transition temperature is uniquely determined by the total bulk anisotropy constant K at zero temperature³⁰. Contributions to K are mainly dipolar anisotropy constant K_{MD} , arising from magnetic dipolar interaction, and fine structure anisotropy (magneto-crystalline anisotropy) K_{FS} , arising from spin-orbit coupling³⁰. With $K_{MD} = -9.2 \times 10^6$ erg/cm³ and $K_{FS} = 9.4 \times 10^6$ erg/cm³ in the bulk hematite, the Morin transition temperature was predicted to be $0.281T_N = 270$ K (Ref.³⁰), very close to the measured bulk value of 258 K (Ref.¹⁷).

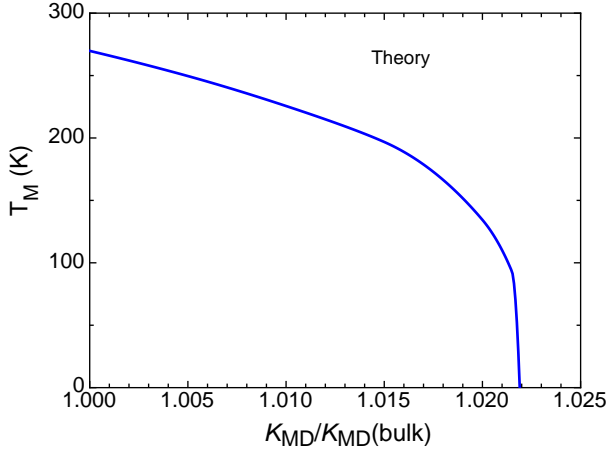


FIG. 12: Numerically calculated T_M as a function of $K_{MD}/K_{MD}(\text{bulk})$, where $K_{MD}(\text{bulk})$ is the bulk anisotropy constant. The calculation is based on a simple model presented in Ref.³⁰ and on the assumption that K_{FS} remains unchanged.

Following this simple model, we can numerically calculate T_M as a function of $K_{MD}/K_{MD}(\text{bulk})$ on the assumption that K_{FS} remains unchanged, where $K_{MD}(\text{bulk})$ is the bulk anisotropy constant. The calculated result is shown in Fig. 12. It is apparent that T_M is suppressed to zero when the magnitude of K_{MD} increases by 2.2%. Near this critical point, T_M decreases rapidly with increasing the magnitude of K_{MD} . For nanotubes, contribution of the surface anisotropy is substantial and should be added to the total anisotropy constant. Following the expressions used in Refs.^{27,28}, we have

$$K_{MD} = K_{MD}(\text{bulk}) + 2K_{s\parallel}/t_{av} + 2K_{s\perp}/L_{av}, \quad (4)$$

where $K_{s\parallel}$ and $K_{s\perp}$ is the surface anisotropy constants for the planes parallel and perpendicular to the c -axis, respectively, and L_{av} is the average tube length. Here we have assumed that the surface areas of the inner and outer walls are the same for simplicity. For the nanotubes, T_M is nearly suppressed to zero. According to Fig. 12, $K_{MD}/K_{MD}(\text{bulk})$ should be close to 1.022 for the nanotubes with $L_{av} = 317$ nm and $t_{av} = 32$ nm. For the nanorings (short nanotubes), the zero-field T_M is about 211 K. This implies that T_M is totally suppressed by 47 K compared with the bulk value of 258 K. Since the finite-size effect can suppress T_M by 22 K (see discussion above), the additional suppression of T_M by 25 K should be due to an increase in K_{MD} by about 0.58% according to Fig. 12, that is, $K_{MD}/K_{MD}(\text{bulk}) = 1.0058$ for the short nanotubes with $L_{av} = 115$ nm and $t_{av} = 58$ nm. Substituting these $K_{MD}/K_{MD}(\text{bulk})$, L_{av} , and t_{av} values of both nanoring and nanotube samples into Eq. 4, we obtain two equations with two unknown variables, $K_{s\parallel}$ and $K_{s\perp}$.

Solving the two equations for the unknown $K_{s\parallel}$ and $K_{s\perp}$ yields $K_{s\parallel} = -0.37$ erg/cm² and $K_{s\perp} = 0.42$ erg/cm². The deduced magnitudes of the surface anisotropy constants are in the same order of the experimental values found for Ni and Co [$K_s = -0.22$ erg/cm² for Ni(111) and 0.5 erg/cm² for Co(0001)]²⁷⁻²⁹. Therefore, the observed intriguing experimental results can be naturally explained by a negative and a positive surface anisotropy constant in the surface planes parallel and perpendicular to the crystalline *c*-axis, respectively.

TABLE II: Some parameters for six nanostructures. The parameters for ellipsoidal, spindle, flattened, and rhombohedral structures are calculated from the data reported in Ref.²². The Fe occupancies for the nanoring and nanotube structures are inferred from the measured saturation magnetizations (see discussion in the text).

	T_M (K)	ϵ (%)	Fe occupancy	c/a
Ellipsoidal	251.4	0.028(1)	0.9600(3)	2.7337(1)
Spindle	245.4	0.063(1)	0.9921(10)	2.7329(1)
Flattened	231.5	-0.132(2)	0.9787(3)	2.7327(1)
Rhombohedral	220.8	0.053(2)	0.9934(16)	2.7340(1)
Nanoring	211	-0.007(25)	1.0	2.7341(5)
Nanotube	<10	-0.028(48)	1.0	2.7381(9)

Now we discuss the shape dependence of the Morin transition temperature observed in other nanostructures²². It was shown that T_M shifted from highest 251.4 K for ellipsoidal to lowest 220.8 K for rhombohedral structure, with intermediate values of T_M for the other two structures. In Table II, we compare some parameters for four nanostructures reported in Ref.²² and two nanostructures reported here. The total lattice strain ϵ is calculated using $\epsilon = 2\epsilon_a + \epsilon_c$, where ϵ_i is the percentage difference in the lattice constant of a nanostructure and the bulk. It is apparent that T_M does not correlate with any of these parameters. For example, the Fe occupancy (0.96) in the ellipsoidal structure is significantly lower than 1.0, but T_M is the highest and close to the bulk value. This implies that the Fe vacancies should have little effect on the Morin transition. We thus believe that the weak shape dependence of the Morin transition observed in the previous work²² should also arise from the opposite signs of the surface magnetic anisotropic constants. The much lower T_M in the rhombohedral structures can be explained as due to a much larger surface area parallel to the *c* axis in the structure, in agreement with the observed HRTEM image²².

IV. CONCLUSION

In summary, we have prepared single-crystalline hematite nanorings and nanotubes using a hydrothermal method. High-resolution transmission electron microscope and selected-area electron diffraction confirm that the axial directions of both nanorings and nanotubes are parallel to the crystalline *c*-axis. Magnetic measurements show that there exists a first-order Morin transition at about 210 K in the nanoring crystals while this transition disappears in nanotube crystals. The current results suggest that the Morin transition depends very strongly on the shape of nanostructures. This strong shape dependence of the Morin transition can be well explained by a negative and a positive surface anisotropy constant in the surface planes parallel and perpendicular to the crystalline *c*-axis, respectively.

Acknowledgment: This work was supported by the National Natural Science Foundation of China (11174165), the Natural Science Foundation of Ningbo (2012A610051), and the K. C. Wong Magna Foundation.

^a wangjun2@nbu.edu.cn

^b gzhao2@calstatela.edu

- ¹ F. J. Morin, Phys. Rev. **78**, 819 (1950).
- ² P. J. Besser and A. H. Morrish, Phys. Lett. **13**, 289 (1964).
- ³ S. Foner and S. J. Williamson, J. Appl. Phys. **36**, 1154 (1965).
- ⁴ T. Hirone, J. Appl. Phys. **36**, 988 (1965).
- ⁵ F. J. Flanders and S. Shtrikman, Solid State Communi. **3**, 285 (1965).
- ⁶ I. E. Dzyaloshinsky, Phys. Chem. Solids **4**, 241 (1958).
- ⁷ F. Huang, G. J. Mankey, M. T. Kief, and R. F. Willis, J. Appl. Phys. **73**, 6760 (1993).
- ⁸ Y. Li and K. Baberschke, Phys. Rev. Lett. **68**, 1208 (1992).
- ⁹ H. J. Elmers, J. Hauschild, H. Hoche, U. Gradmann, H. Bethge, D. Heuer, and U. Kohler, Phys. Rev. Lett. **73**, 898 (1994).
- ¹⁰ C. M. Schneider, P. Bressler, P. Schuster, J. Kirschner, J. J. de Miguel, and R. Miranda, Phys. Rev. Lett. **64**, 1059 (1990).
- ¹¹ Z. X. Tang, C. M. Sorensen, and K. J. Klabounde, Phys. Rev. Lett. **67**, 3602 (1991).

¹² Y.W. Du, M. X. Xu, J.Wu, Y. B. Dhi, H. X. Lu, and R. H. Xue, *J. Appl. Phys.* **70**, 5903 (1991).

¹³ J. Wang, W. Wu, F. Zhao, and G. M. Zhao, *Appl. Phys. Lett.* **98**, 083107 (2011).

¹⁴ J. Wang, W. Wu, F. Zhao, and G. M. Zhao, *Phys. Rev. B* **84**, 174440 (2011).

¹⁵ J. Wang, F. Zhao, W. Wu, and G. M. Zhao, *J. Appl. Phys.* **110**, 123909 (2011).

¹⁶ M. E. Fisher and M. N. Barber, *Phys Rev Lett* **28**, 1516 (1972).

¹⁷ D. Schroeer and R. C. Nininger, Jr., *Phys. Rev. Lett.* **19**, 632 (1967).

¹⁸ P. K. Gallagher and E. M. Gyorgy, *Phys. Rev.* **180**, 622 (1969)

¹⁹ G. J. Muench, S. Arajs, and E. Matijevic, *Phys. Stat. Sol.* **92**, 187 (1985).

²⁰ A. H. Morrish, *Canted Antiferromagnetism: Hematite* (World Scientific, Singapore, 1994).

²¹ F. Bodker, F. F. Hansen, C. B. Koch, K. Lefmann, S. Mrup, *Phys. Rev. B* **61**, 6826 (2000).

²² S. Mitra, S. Das, S. Basu, P. Sahu, K. Mandal, *J. Magn. Magn. Mater.* **321**, 2925 (2009).

²³ Chun-Jiang Jia *et al.*, *J. Am. Chem. Soc.* **130** **at**, 16968 (2008).

²⁴ A. H. Hill, F. Jiao, P. G. Bruce, A. Harrison, W. Kockelmann, and C. Ritter, *Chem. Mater.* **20**, 4891(2008).

²⁵ G. K. Williamson and W. H. Hall, *Acta Metallurgica* **1**, 22(1953)

²⁶ C. S. Smith and E. E. Stickley, *Phys. Rev.* **64**, 191(1943).

²⁷ U. Gradmann, R. Bergholz, and E. Bergter, *IEEE Trans. Magn.* **Mag-20**, 1840 (1984). The sign of the surface anisotropy constant in the original paper is incorrect, as pointed out in Ref.²⁸. The correct sign was also quoted in Ref.²⁹

²⁸ C. Chappert, K. Le Dang, P. Beauvillain, H. Hurdequin, and D. Renard, *Phys. Rev. B* **34**, 3192 (1986).

²⁹ P. Bruno, *J. Appl. Phys.* **64**, 3153 (1988).

³⁰ J. O. Artman, J. C. Murphy, and S. Foner, *Phys. Rev.* **138**, A912 (1965).